Full length article

Sequential obstacle interactions with dislocations in a planar array

Shuozhi Xu [a, *], David L. McDowell [b, c], Irene J. Beyerlein [a, d]

[a] California NanoSystems Institute, University of California, Santa Barbara, Santa Barbara, CA 93106-6105, USA
[b] GWW School of Mechanical Engineering, Georgia Institute of Technology, Atlanta, GA 30332-0405, USA
[c] School of Materials Science and Engineering, Georgia Institute of Technology, Atlanta, GA 30332-0245, USA
[d] Department of Mechanical Engineering, Materials Department, University of California, Santa Barbara, Santa Barbara, CA 93106, USA

ABSTRACT

The strengthening of metals by nano-scale obstacles is mainly attributed to the impediment to glide dislocations offered by these obstacles. It is important to understand the mechanisms for dislocation bypass of obstacles having nano-scale dimension, including the atomic-scale structure changes sustained by both obstacles and dislocations after the bypass process. Recently, atomic-scale modeling has provided much insight into obstacle interactions involving a single dislocation. However, the more naturally occurring scenarios involving a sequence of encounters with arrays of moving dislocations are not as well understood owing to prohibitively large length scale requirements for atomistic models. In this study, we utilize a novel multiscale concurrent atomistic-continuum method to simulate a sequence of interactions between glide dislocations in an array with a spherical nano-obstacle (either a void or an impenetrable precipitate) in Al. In the case of a void, the bypassing array of dislocations progressively weakens the void until it splits the originally spherical void into two hemispheres. In the case of a large impenetrable precipitate, sequential dislocations in the array bypass via alternating mechanisms of Orowan looping and Hirsch looping. The residual dislocation loop created around the precipitate by the bypass of the first dislocation is completely removed by the passage of the subsequent dislocation. These mechanisms can benefit the design of materials that are reinforced with nanophase inhomogeneities to achieve ultra high strength.

© 2019 Acta Materialia Inc. Published by Elsevier Ltd. All rights reserved.

1. Introduction

The strength of crystalline materials is governed by the motion of dislocations, which tend to move in arrays on a preferred slip plane for many practical alloy systems with low to medium intrinsic stacking fault energy (ISFE). One of the most effective methods for strengthening crystalline materials is to introduce small obstacles with nanoscale dimensions [1]. These obstacles are typically immobile and are introduced into individual crystals by alloying, quenching, or irradiation [2]. When the material is deformed, stress drives dislocations to these obstacles and a higher stress level is needed for dislocation bypass. The higher the additional stress, the more effective is the obstacle at strengthening. Thus, design of high-performance, high-strength materials relies on understanding the effectiveness of nm-sized obstacles to hindering or blocking motion of dislocation arrays. For nearly a century, the literature reflects conventional understanding of a single dislocation interacting with an obstacle [3]. However, the effect of the interaction between the first dislocation and the obstacle on subsequent dislocation/obstacle interactions is less well understood.

When the obstacle is a void, two edge dislocation/void interaction mechanisms exist for mid-plane encounters, distinguished by whether or not the dislocation climbs, as illustrated in Fig. 1. In both mechanisms, the dislocation, with Burgers vector magnitude b, creates two surface steps with size b on the 'incoming' and 'outgoing' sides of the void. However, the outgoing surface step forms either on the original slip plane (Fig. 1 (c1)) or on a slip plane that is h' away from the original one as a result of dislocation climb (Fig. 1(c2)), which tends to occur when it is easy for jogs to form along a dislocation line [4]. In previous atomistic simulations of dislocation/void interactions, dislocation climb was observed in body-centered cubic (BCC) Fe, W, and Mo [4,5], but not in face-centered cubic (FCC) Cu [6]. The dissociation of dislocations into Shockley partials in FCC metals increases dislocation climb energy barrier because both partial dislocations need to climb to complete

* Corresponding author.
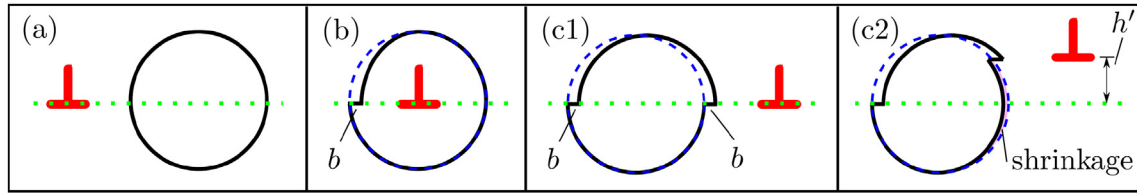 *E-mail address:* shuozhixu@ucsb.edu (S. Xu).

Fig. 1. Illustrations of two edge dislocation/void interaction mechanisms, distinguished by whether or not the dislocation undergoes a climb process. The green dotted line is the original slip plane; the black solid and blue dashed circles are the current and original void shape, respectively. In both mechanisms, the dislocation creates two surface steps with magnitude b on the incoming and outgoing sides of the void, respectively. In (c1), the dislocation does not climb and the outgoing surface step forms on the original slip plane; in (c2), the dislocation climbs by h' with respect to the original slip plane by absorbing some vacancies from the void, leaving behind a surface step on the outgoing slip plane. In (c2), the void shrinks by the violet area (denoted "shrinkage"). Note that in 3D, a jog is formed on the dislocation line in (c2). (For interpretation of the references to color in this figure legend, the reader is referred to the Web version of this article.)

the climb of the extended dislocation [7]. Indeed, it was found that the probability of dislocation climb in an FCC metal increases with higher ISFE, especially when the center of the void is located on the compressive side of the edge dislocation [8,9]. Bacon et al. [3] predicted that an edge dislocation may climb upon exiting a void in FCC metals with medium to high ISFE, such as Al. Hence, it would be interesting to test this hypothesis by modeling dislocation/void interactions in Al.

Obstacles other than voids may not be sheared by glide dislocations. In the literature, there exist two main interaction mechanisms between a dislocation and an impenetrable precipitate. Based on continuum linear elastic dislocation theory, Mott and Nabarro [10] and Orowan [11] proposed that each interacting dislocation leaves behind an Orowan shear loop, and so the bypass of a sequence of glide dislocations results in a set of concentric shear loops around the precipitate. This multi-dislocation interaction scenario, which is the same for dislocations with any character angle, leads to what is known as Orowan strain hardening. Humphreys and Hirsch [12] proposed an alternative mechanism in which, if all dislocations are edge-oriented, each dislocation/precipitate interaction leads to two pairs of prismatic loops, one on each side of the obstacle. This multi-dislocation interaction, which involves the cross-slip of the screw components of dislocations, is known as Hirsch looping. Both Orowan and Hirsch looping are

illustrated in Fig. 2. Post-mortem experimental studies diverge in their support of such theories, with some observing both Orowan shear loops and Hirsch prismatic loops while others reporting neither type of residual defect [12–15].

Continuum-based modeling techniques such as discrete dislocation dynamics (DDD), level-set method, phase-field modeling, and larger scale crystal plasticity have been used to model dislocation/precipitate interactions. These continuum-based models typically assume that the bypass mechanism does not change as more dislocations interact with the precipitate. For example, in DDD simulations, when an array of edge dislocations sequentially bypasses an impenetrable precipitate, either Orowan looping [16–18] or Hirsch looping [19] occurs, depending on whether cross-slip is permitted. As revealed by level-set-based [20,21] and DDD simulations [22], the specific looping mechanism also depends on the interplanar distance h between the slip plane and the plane containing the precipitate center, as well as the coherency stress (due to the mismatch in elastic properties between the matrix and precipitate) and image stress (due to the change in the strain energy of a dislocation near a second-phase precipitate).

The mechanisms by which dislocations overcome nano-scale obstacles necessarily involve potentially significant atomic-scale structural changes in both the obstacle and dislocation during the interaction. Thus, atomic-scale calculations via either molecular
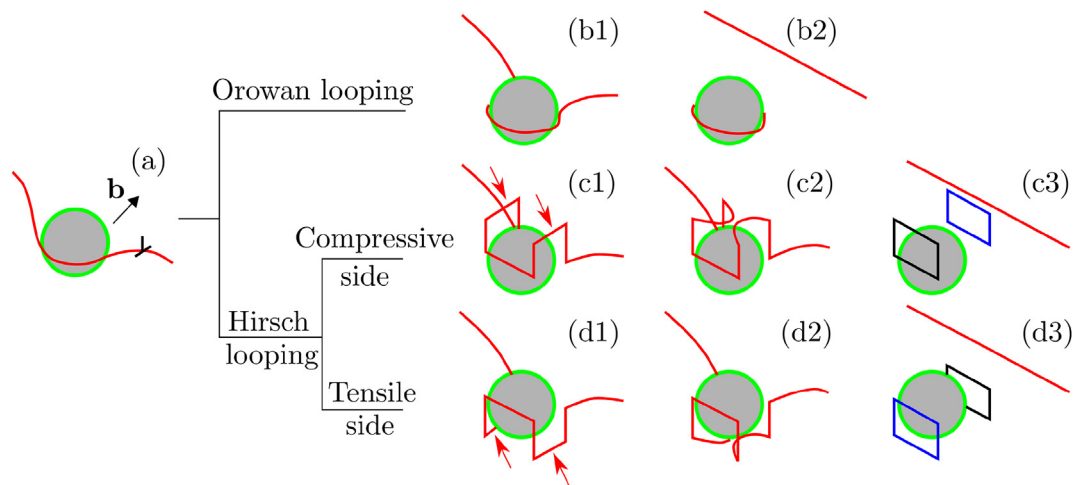

Fig. 2. Illustrations of two dislocation/impenetrable precipitate interaction mechanisms: Orowan looping and Hirsch looping. Other mechanisms may apply if the precipitate is too small. In (a), the red curve is the edge dislocation, with its extra half-plane above the slip plane. Hence, the compressive and tensile sides of the dislocation stress field lie above and below the slip plane, respectively. In Orowan looping, the dislocation bows around the precipitate in (b1) and a shear loop is left behind in (b2). In Hirsch looping, the screw components (red arrows) of the dislocation cross slip toward the (c1) compressive or (d1) tensile side of the original slip plane; in (c2) and (d2), the two screw dislocation segments with the same Burgers vector but opposite line directions move together to annihilate each other; in (c3) and (d3), edge prismatic loops of interstitial (in black) and vacancy (in blue) types are formed. Note that (b1) and (b2) hold for dislocations with any character angle in Orowan looping, while the illustrated Hirsch looping mechanism only applies to edge dislocations. (For interpretation of the references to color in this figure legend, the reader is referred to the Web version of this article.)

dynamics (MD) or molecular statics (MS) methods are the most suitable predictive approaches for exploring possible interaction mechanisms. Based on MD simulations in Ni, Proville and Bakó [23] observed that the second dislocation, after bypassing a Ni₃Al coherent precipitate (1.5 nm radius) with an Orowan loop, formed two jogs but the state of the original Orowan loop was not described. Using MS for Mg, Groh [24] studied the interaction of a second basal dislocation with an impenetrable obstacle (2 nm radius) wrapped by an Orowan loop and observed Hirsch looping, in which the Orowan loop was removed by formation of prismatic loops. The second glide dislocation also formed jogs and transported the prismatic loop away from the obstacle. However, interaction mechanisms of subsequent dislocations were not explored. By studying an impenetrable obstacle (1.5 nm radius) in Cu via the MD method, Hatano [25] found that the Hirsch looping mechanism is favored over the Orowan looping if the local stress field is asymmetric with respect to the slip plane, which may be the case if the externally applied stress is asymmetric with respect to this configuration or h is too large; after Hirsch looping, the dislocations that glide away contained jogs and left a row of sessile prismatic loops behind. Taken together, these results suggest that the interaction mechanisms of an obstacle with an array of moving dislocations cannot be understood based on only a single dislocation/precipitate interaction. In particular, it is common practice to extrapolate such that these same interactions are assumed to occur repeatedly with each successive dislocation and the obstacle remains unchanged. On the other hand, direct observation by experimental techniques during deformation at the needed time and length scales are extremely challenging, at the present time, and have not shed sufficient light on understanding of sequential bypass mechanisms. In addition, large scale atomistic simulations of sequential obstacle interactions with dislocations have been limited to date, since they would be too computationally intensive owing to the long range nature of the stress field in a dislocation array [26,27].

Recently, a novel concurrent atomistic-continuum (CAC) approach was developed to increase the length scale that can be addressed using atomic-scale simulations. The CAC method employs a unified atomistic-continuum integral formulation, with the underlying interatomic potential as the only constitutive rule [28]. In contrast to most other atomistic/continuum coupling multiscale materials modeling approaches, CAC features a two-way exchange of dislocations between the atomistic and coarse-grained domains without having to apply mesh refinement to the latter [29]. It is

useful for problems in which full atomistic resolution is required only in some regions (e.g., near obstacles), with coarse-graining employed elsewhere to support representation of the long-range stress fields of moving dislocation arrays [30]; in particular, CAC has been applied to slip transfer of sequential dislocations across a Σ3{111} coherent twin boundary and a Σ11{113} symmetric tilt grain boundary [31,32]. In this work, we employ the CAC method to examine the favorable bypass mechanisms used by moving arrays of dislocations to overcome nano-scale obstacles.

To build more comprehensive understanding, we analyze two extreme cases, one in which the obstacle is significantly more compliant than the matrix (i.e., a void), and the other in which the obstacle is much stiffer (i.e., an impenetrable precipitate). While seemingly hypothetical, these two cases are common in many materials [33,34]. We show that for an order of magnitude range in void diameter (0.56 nm ≤ D ≤ 5.6 nm), the void retains its size but accumulates steps after successive interactions with dislocations in a planar array; moreover, the strength of a sheared void decreases as the number of accumulated steps increases. A fully split void weakly hinders subsequent dislocation motion. In the case of an impenetrable precipitate (D ≥ 1.12 nm), a repeated sequence of dislocation interactions is observed that leaves the glide dislocation and obstacle free of residual debris. This is accomplished by formation of an Orowan loop after the bypass of the first dislocation, followed by its removal after the bypass of the second dislocation via the Hirsch looping mechanism.

2. Methodology

Fig. 3 shows the computational model for sequential dislocation/obstacle interactions. The problem is partitioned into an atomistic domain and a coarse-grained domain [35]. In the former, atomic positions are updated in the same way as in MD or MS, whereas in the latter, neither displacement continuity nor strain compatibility is required between finite elements. As a result, discontinuities may form between finite elements, allowing for nucleation and propagation of displacement discontinuities (e.g., dislocations and intrinsic stacking faults) through a lattice [36]. In this work, 3D rhombohedral second nearest neighbor finite elements with all faces on the {111} planes are adopted for an FCC lattice [37]. Atoms are filled in at jagged interstices along the boundary to facilitate application of periodic boundary conditions (PBCs) along the x direction, while all other cell boundaries are assumed traction-free. The simulation cell size lies within a
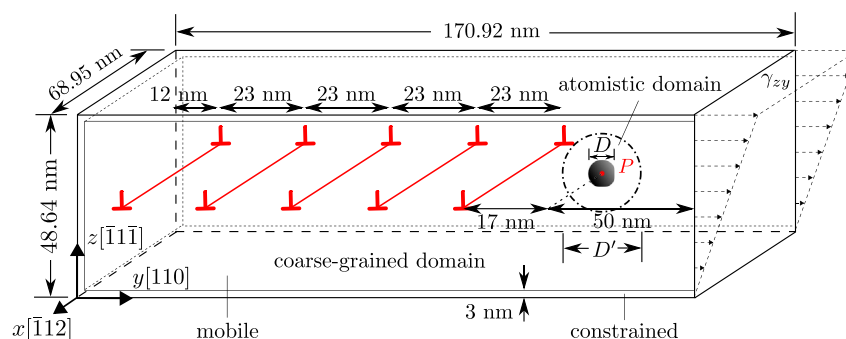

Fig. 3. Illustration of the simulation cell for interactions between five edge dislocations in a planar array and an obstacle (filled black sphere centered at the red point P with diameter D), which is either a void or an impenetrable precipitate. An atomistic domain is meshed within a sphere centered at P with diameter D' to let the obstacle deform and dislocations evolve at full atomic resolution, while the coarse-grained domain with 3D rhombohedral elements is employed elsewhere. Five initially equally spaced edge dislocations in the coarse-grained domain having the same Burgers vector $\mathbf{b} = (a_0/2)[110]$ are placed on the same $(\bar{1}1\bar{1})$ slip plane. Note that (i) owing to the PBCs applied along the x direction, the dislocations are infinitely long and the obstacles form an infinitely long periodic array, and (ii) after energy minimization, the dislocations become dissociated and are no longer equally spaced along the y direction, as expected. (For interpretation of the references to color in this figure legend, the reader is referred to the Web version of this article.)

68.95 nm $\times$ 170.92 nm $\times$ 48.64 nm cuboid with lattice orientations of $x[\overline{1}12]$, $y[110]$, and $z[\overline{1}1\overline{1}]$. It contains about 14,500 elements with 2197 atoms per element and about 2.8 million atoms, i.e., about 2.9 million degrees of freedom. Note that an equivalent full atomistic model would contain about 35 million atoms.

In all simulations, the obstacle, either a void or an impenetrable precipitate, is assigned a spherical shape with diameter D. In the cell, it is centered at point P, which is set at 50 nm from the rightmost cell boundary along the y direction and equidistant in the x and z directions from the cell boundaries. First, all finite elements within a sphere centered with a diameter D' are refined to the atomic scale, to let the obstacle deform and dislocations evolve freely [38]. $D' = 4D$ and $8D$ for the void and the precipitate, respectively. To create a void, all atoms within a sphere with diameter D are removed. To create an impenetrable precipitate, all atoms within a sphere with diameter D are affinely deformed following the simulation cell, yet their interatomic forces are zeroed at each step.

Interactions are sensitive to obstacle size and so this study considers obstacle sizes spanning an order of magnitude, i.e., from 0.56 to 5.6 nm. Table 1 summarizes N_{obs}, the number of atoms deleted to form a void or the number of atoms belonging to the precipitate. The upper range of D selected for the present calculations (i.e., 5.6 nm) is defined such that no superfluous dislocations will nucleate under the stresses applied in our simulations. The computational analysis used to select these sizes is described in Appendix A.

Next, an array of N_{dis} identical, like-signed, edge dislocations is placed in front of the obstacle. This means they have the same Burgers vector $\mathbf{b} = (a_0/2)[110]$ and lie on the same $(\overline{1}1\overline{1})$ slip plane. The array is created by applying the corresponding isotropic displacement fields to all atoms/nodes [39]. In most simulations, $N_{dis} = 5$, but in some cases, as we will explain later, N_{dis} may have a smaller value. Initially, the dislocations are straight and equally spaced by 23 nm, with the leftmost one located 12 nm from the leftmost cell boundary and the rightmost one 17 nm from the obstacle center P. Since PBCs are applied along the x direction, the dislocations are infinitely long and the obstacles form an infinitely long periodic array, as previously mentioned.

The material chosen for this study is FCC Al for its near ideal isotropic elasticity [40]. Its lattice parameter is $a_0 = 4.05$ Å. The calculations employ the embedded-atom method interatomic potential by Mishin et al. [41]. As discussed in Section 1, the coherency/image stresses and the asymmetry of the local stress field may influence the dislocation/obstacle interactions [20–22,25]. To minimize these effects, in our idealized models, (i) the coherency/image stresses are removed by letting the material for the impenetrable obstacle be Al, and (ii) the slip plane passes, or lies at most $d_{111}/2$ from, the obstacle center, where $d_{111} = a_0/\sqrt{3}$ is the interplanar distance between two adjacent {111} planes. As will be discussed in Section 3.2, the distance between the slip plane and the plane containing the obstacle center becomes non-negligible when D reduces to 0.56 nm, and the corresponding dislocation/precipitate interaction mechanism differs from those for larger D.

All CAC simulations are carried out using PyCAC [42,43]. Atoms/nodes within 3 nm from the upper, lower, and leftmost boundaries are allowed to move within the x-z plane, but not along the y

direction. First, a quasistatic CAC simulation with the conjugate gradient algorithm [37] is performed to attain stable dislocation cores and obstacle configurations. After energy minimization, the dislocations are no longer equally spaced along the y direction but are distributed as a result of the constraints imposed by the leftmost boundary, the obstacle, and the Peierls barrier. Then, in a dynamic CAC simulation, a homogeneous simple shear strain γ_{zy} is applied on the cell to drive the dislocations towards the obstacle. The strain rate is 10^7 s^{-1} and the timestep size is 5 fs. Note that CAC simulations allow for a larger timestep size than MD simulations [1,38], as validated in Appendix B. After each deformation increment step, the atoms at the rightmost boundary are not restrained and therefore all glide dislocations can exit the cell after bypassing the obstacle. These calculations are carried out using an NVT ensemble, with a constant temperature 10 K maintained via Langevin dynamics. Simulation results are visualized using OVITO [44], with the defects identified by the adaptive common neighbor analysis (a-CNA) method [45].

3. Results and discussion

3.1. Dislocation/void interactions

When a dislocation meets a void, one of two mechanisms are possible for mid-plane encounters, as illustrated in Fig. 1. In CAC simulations, for all N_{dis} dislocations and all void sizes D, we find that dislocation climb does not occur, in agreement with a recent MD simulation in Al and Al–Mg alloy [46]. These climb-free interactions allow for direct comparisons between CAC simulations and analytic continuum models of dislocation shearing, most of which consider the interaction between an isolated dislocation impinging on an unsheared spherical or circular void. In sequential dislocation/void interactions, however, the void is unsheared only for the first incoming dislocation, whose interaction with the void is found to follow the conventional process for all void size D, i.e., the portion of the dislocation that comes in contact with the void shears the void, while the two non-contacting segments of the dislocation continue to glide and travel around the void. These two gliding arms of the dislocation come into contact with each other and annihilate. This event marks a critical breaking point in which the two moving parts of the dislocation reconnect to continue glide, virtually unaltered, on the same glide plane. The included angle formed between two dislocation segments at this point is referred to as the depinning angle, ϕ_c, as illustrated in Fig. 4. At the depinning point, the applied resolved shear stress is taken as the depinning stress, τ_c. The dislocation leaves two steps of size b on the surface of the void, with no void shrinkage. For example, in Fig. 5, the original spherical void with $D = 3.36$ nm contains 1214 vacancies, and the deformed, two hemispherical half voids, which are slightly shifted by b, contain 602 and 612 vacancies, respectively.

Fig. 6 shows that the depinning stress for the first dislocation depends on both N_{dis} and D. Thus, we refer to the depinning stress as $\tau_{c,N_{dis}}$ in what follows. As D increases, a larger portion of the dislocation segment must shear the void before the dislocation can reconnect with itself and breakaway. Hence, the larger the void, the larger $\tau_{c,N_{dis}}$, as would be intuitively expected. In addition, continuum models [47] predict that the lower the depinning stress, the larger the depinning angle, which is confirmed in Fig. 5.

For a planar dislocation array, the effect of void size D on $\tau_{c,N_{dis}}$ for the first dislocation encountering the void can be treated analytically using linear elasticity dislocation theory. A unit dislocation segment (the green box in Fig. 4) moving along $\mathbf{d}$ with length $\mathbf{l}$ and Burgers vector $\mathbf{b}$ experiences an applied force $\mathbf{F}_{app}$, the total force imposed by all other dislocations in the array $\mathbf{F}_{dis}$, resistance

Table 1
N_{obs}, the number of atoms deleted to form a void or the number of atoms within a precipitate, for different obstacle diameter D.

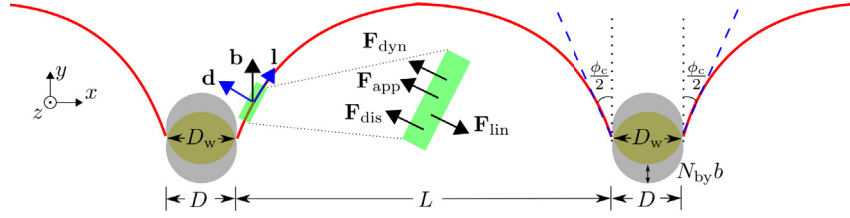| D (nm)	0.56	1.12	2.24	3.36	4.48	5.6
N_{obs}	7	39	362	1214	2841	5596

Fig. 4. Illustration of the critical dislocation depinning configuration when the dislocation is about to exit a void. Projected on the slip plane, two hemispheres of the original spherical void with initial diameter D are shifted against each other by $N_{by}b$ after N_{by} dislocation bypasses; the yellow shaded lenticular region is the overlapped section between the two hemispheres. $\mathbf{b}$ is the Burgers vector of the dislocation, $\mathbf{l}$ is the unit vector along the dislocation line, $\mathbf{d}(\perp\mathbf{l})$ is the unit vector along the dislocation moving direction, L is the intervoid ligament distance, D is the initial void diameter, and ϕ_c is the depinning angle. (For interpretation of the references to color in this figure legend, the reader is referred to the Web version of this article.)
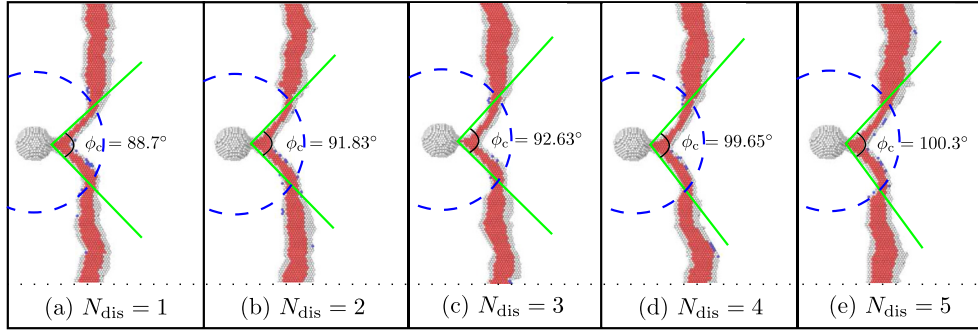

Fig. 5. Snapshots of the first edge dislocation exiting a void with $D = 3.36$ nm when N_{dis} varies from 1 to 5. The region inside the blue dashed arc is atomistically resolved; the angle formed between the two green lines is the depinning angle ϕ_c. Atoms are colored by a-CNA [45], with BCC, hexagonal close-packed, and disordered local structures in blue, red, and white, respectively; all FCC atoms are deleted. The same color scheme is used in all snapshots in the remainder of this paper, unless stated otherwise. (For interpretation of the references to color in this figure legend, the reader is referred to the Web version of this article.)
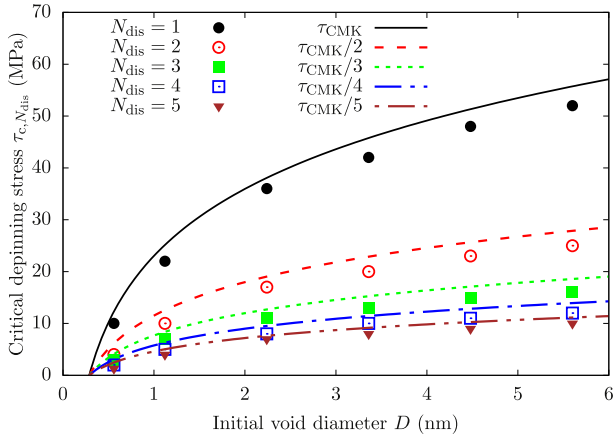

Fig. 6. CAC-based depinning stress with respect to the initial void diameter D taken at the first dislocation exiting the void when N_{dis} varies from 1 to 5. The predictions by Eq. (13) are also shown.

from dislocation line tension $\mathbf{F}_{lin}$, and dynamics-induced force $\mathbf{F}_{dyn}$ which represents the combined effects of phonon/electron dragging, radiation friction, inertial effects [48], etc. At the depinning configuration, a balance of forces yields

$$\mathbf{F}_{app} + \mathbf{F}_{dis} + \mathbf{F}_{dyn} - \mathbf{F}_{lin} = 0 \tag{1}$$

where the first two forces can be expressed using the Peach-Koehler formula following [49].

$$\mathbf{F}_{app} = (\boldsymbol{\sigma}_{app} \cdot \mathbf{b}) \times \mathbf{l} = \tau_{c,N_{dis}} b\mathbf{d} \tag{2}$$

$$\mathbf{F}_{dis} = \left(\sum_{i}^{N_{dis}-1} \boldsymbol{\sigma}_i \cdot \mathbf{b} \right) \times \mathbf{l} \tag{3}$$

where $\boldsymbol{\sigma}_{app}$ is the applied stress tensor and $\boldsymbol{\sigma}_i$ is the stress tensor at the first dislocation caused by the ith dislocation in its wake. In addition,

$$\mathbf{F}_{lin} \approx \kappa\Gamma\mathbf{d} \tag{4}$$

where Γ is the dislocation line tension (in units of energy per unit length) and κ is the local curvature of the unit dislocation segment (in units of per unit length). Assume that the bow-out dislocation configuration forms an arc-shape, i.e., $\kappa \approx 2\cos(\phi_c/2)/L$ and the gliding edge dislocation obtains near-screw character. Then a first-order estimate of the line tension of an undissociated screw dislocation is the dislocation line energy, i.e. [50],

$$\Gamma = \frac{\mu b^2}{4\pi} \ln\left(\frac{R_0}{r_0}\right) \tag{5}$$

where elastic isotropy has been assumed, μ is the isotropic equivalent shear modulus, R_0 and r_0 are the radii of the dislocation strain field and dislocation core, respectively. Following Bacon et al. [51], we take $R_0 = \overline{D} = (D^{-1} + L^{-1})^{-1}$ and $r_0 = b$, where the intervoid ligament distance L equals the simulation cell edge length along the x direction minus D. Note that both D and L affect dislocation line tension. Therefore, the depinning stress, for the interaction with the first incoming dislocation in a planar array of N_{dis} dislocations, is

$$\tau_{c,N_{dis}} = \frac{\mu b \cos(\phi_c/2)}{2\pi L} \ln\left(\frac{\overline{D}}{b}\right) - \frac{\left|\mathbf{F}_{dis} + \mathbf{F}_{dyn}\right|}{b} \quad (6)$$

In most continuum models, a dislocation quasi-statically by-passes a void in the absence of other dislocations; hence, $N_{dis} = 1$, and both $\mathbf{F}_{dyn}$ and $\mathbf{F}_{dis}$ are zero. It follows that Eq. (6) becomes

$$\tau_{c,1} = \frac{\mu b \cos(\phi_c/2)}{2\pi L} \ln\left(\frac{\overline{D}}{b}\right) \quad (7)$$

In reality, however, ϕ_c is usually unknown *a priori*. Bacon et al. [51] and Scattergood and Bacon (SB) [52] assumed that the depinning only occurs when $\phi_c = 0$, which gives

$$\tau_{SB} = \frac{\mu b}{2\pi L} \ln\left(\frac{\overline{D}}{b} + \Delta\right) \quad (8)$$

where the constant $\Delta = 1.52$ is related to the surface energy of the void [53]. Recently, Crone, Munday, and Knap (CMK) [54] more accurately accounted for the image forces on the dislocation due to the free surface of the void and proposed a slightly modified model, i.e.,

$$\tau_{CMK} = \frac{\mu b}{2\pi(L + D/2)} \ln\left(\frac{\overline{D}}{b}\right) \quad (9)$$

which was shown to provide good agreement with numerical simulations based on DDD [54] and CAC [55,56]. Thus, the CMK model will be used for dislocation/void interactions in what follows.

Fig. 6 shows that τ_{CMK} captures well the void size effect, only slightly overestimating the CAC-based $\tau_{c,1}$. The agreement is good considering that Eq. (9) omits dislocation dynamic effects and makes simplifying assumptions in calculating line tension and curvature. However, as N_{dis} increases, the depinning stress for the first dislocation decreases significantly and τ_{CMK} differs greatly from CAC-based predictions. The discrepancy is mainly attributed to the lack of $\mathbf{F}_{dis}$ in Eq. (9). When $N_{dis} > 1$, all dislocations have the same Burgers vector and glide on the same slip plane. As such, the dislocations in the wake of the first one apply a repulsive force on the latter, $\mathbf{F}_{dis}$, that pushes the dislocation forward. Calculating $\mathbf{F}_{dis}$ requires knowing the positions of all other dislocations in the array when the first dislocation interacts with the void. A reasonable approximation can be obtained by considering the equilibrium static positions of the dislocations in a single-ended pile-up. Based on static continuum elasticity theories, Eshelby et al. [57] showed that the stress on the leading dislocation equals the applied stress multiplied by the number of dislocations in the same pile-up, i.e.,

$$\mathbf{F}_{app} + \mathbf{F}_{dis} = N_{dis}\mathbf{F}_{app} \quad (10)$$

which can be re-written as

$$\mathbf{F}_{dis} = (N_{dis} - 1)\mathbf{F}_{app} = (N_{dis} - 1)\tau_{c,N_{dis}}b\mathbf{d} \quad (11)$$

Substituting Eq. (11) into Eq. (6) yields

$$\tau_{c,N_{dis}} = \frac{1}{N_{dis}}\left[\frac{\mu b \kappa}{4\pi} \ln\left(\frac{\overline{D}}{b}\right) - \frac{\left|\mathbf{F}_{dyn}\right|}{b}\right] \quad (12)$$

which suggests that the effect of the dislocation array is to divide the depinning stress by N_{dis}. The same formulation can be applied to Eq. (9), giving

$$\tau_{CMK,N_{dis}} = \frac{\tau_{CMK}}{N_{dis}} = \frac{\mu b}{2\pi N_{dis}(L + D/2)} \ln\left(\frac{\overline{D}}{b}\right) \quad (13)$$

It is worth noting that in formulating Eq. (13), (i) $\mathbf{F}_{dyn}$ is still omitted, which would lead to an overestimate of the depinning stress, and (ii) actual $\mathbf{F}_{dis}$ may be lower than the prediction of Eq. (11) since dislocations in a moving array in front of a shearable void glide farther apart than those in a static single-ended pile-up, resulting in an underestimation of the depinning stress. Despite these, Fig. 6 shows that $\tau_{CMK,N_{dis}}$ better predicts the depinning stress when $N_{dis} > 1$ than τ_{CMK} (Eq. (9)).

Next, we investigate subsequent dislocation interactions with the sheared void and depinning stresses required for these dislocations to bypass. Similar to the first dislocation, each sequential dislocation shears the void by the same amount b, despite the fact that the void has been damaged by the passage of preceding dislocations. This finding implies that the number of sequential dislocations in an array needed to completely split the original spherical void into two separated, hemispherical voids equals $\lceil D/b \rceil$, provided that the void incurs no additional changes in shape or size. Indeed, when $D = 0.56$ and 1.12 nm, the void is completely split into two halves after the second and the fourth dislocation passage, respectively, as shown in Fig. 7. When $D = 5.6$ nm, after being sheared by five sequential moving edge dislocations, the original void acquires two surface steps, each of which has size $5b$, and thus, it has evolved into two hemispheres that are shifted against each other but not separated, as shown in Fig. 8. Completely splitting this void would require in total 20 bypassing dislocations.

The depinning stress $\tau_{c,N_{dis}}$ of each subsequent dislocation with the already sheared void is, however, neither the same as the first dislocation with the perfect void nor the same as the dislocation before it. Following sequential dislocation bypass, the forces applied on the interacting dislocation by other dislocations in the same array, i.e., $\mathbf{F}_{dis}$, rapidly decreases to zero and then becomes negative, leading to an increase in $\tau_{c,N_{dis}}$. This trend is a combined result of the fact that (i) there are fewer dislocations on the incoming side of the void and (ii) the dislocations that have already bypassed the void exert a back stress on the ones that have yet to bypass. Thus, based on $\mathbf{F}_{dis}$ alone, it would be expected that $\tau_{c,N_{dis}}$ increases as more dislocations bypass the void.

However, Fig. 9(a) shows that, with each passing dislocation, $\tau_{c,N_{dis}}$ decreases. Hence, the change in the void shape must contribute to the decrease of $\tau_{c,N_{dis}}$, so much so that it outweighs the opposing effect of a decreasing $\mathbf{F}_{dis}$. As illustrated in Fig. 4, the sheared void with surface steps can be described as two adjacent hemispherical voids that share a common lenticular region that still intersects the glide plane. After each dislocation bypass, two geometric parameters change: the effective diameter D_w and the perimeter of the shared region. In Fig. 9(a) and (b), respectively, $\tau_{c,5}$ is plotted with respect to D and D_w. Nevertheless, the differences between the two plots are relatively small, suggesting that the change in D_w does not significantly influence $\tau_{c,N_{dis}}$. Therefore, the change in the other geometric parameter, i.e., the perimeter of the shared region, is considered to play a leading role in decreasing $\tau_{c,N_{dis}}$ as more dislocations bypass the void. This argument is reasonable because this perimeter is proportional to the work required by the dislocation to pass the void [54].

Taken together, our CAC calculations regarding sequential interactions of dislocations in a planar array with a void indicate that the depinning state depends on the void morphology, dynamic effects, and the number/positions of gliding dislocations on both sides of the void. These factors are omitted in conventional continuum dislocation/void interaction models (e.g., Eq. (9)), which only include one parameter D to represent the void geometry and
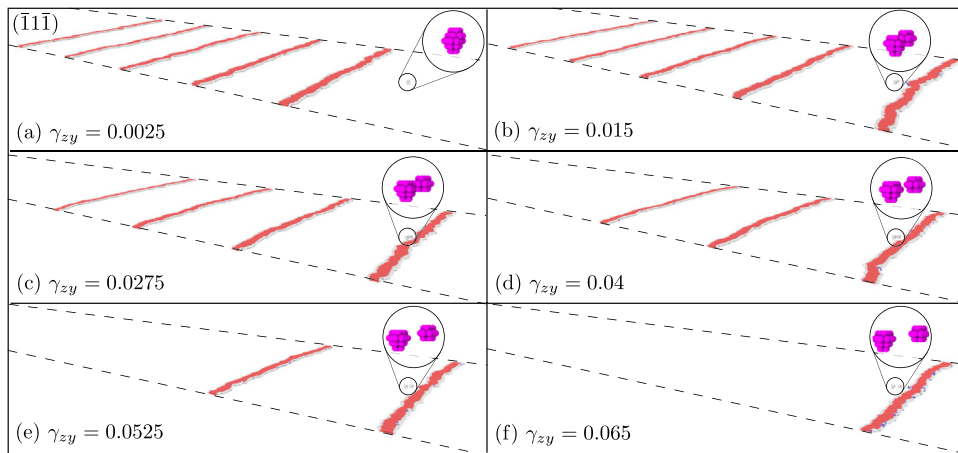
Fig. 7. Snapshots of five edge dislocations sequentially bypassing a void with $D = 0.56$ nm. After bypassed by the second dislocation, shown in (c), the original spherical void, which contains seven vacancies, is split into two smaller hemispherical voids, with the left and right ones containing four and three vacancies, respectively. In the insets, atoms on the void surface are in magenta.
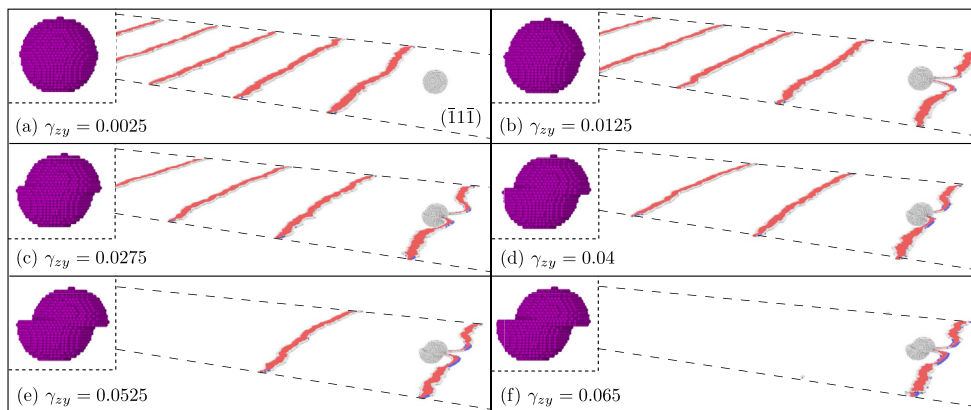

Fig. 8. Snapshots of five edge dislocations sequentially bypassing a void with $D = 5.6$ nm. After each dislocation bypass, two steps are created on the surface of the void. In the insets, atoms on the void surface are in magenta.

assume a single dislocation glides quasi-statically in the material. The expression presented here, Eq. (13), extends understanding of previous continuum models to include the effect of an array of dislocations, while also excluding the dynamic effects.

3.2. Dislocation/precipitate interactions

Two distinct mechanisms for dislocation bypass — Orowan looping and Hirsch looping — exist for the unit process of single dislocation/impenetrable precipitate interactions, as illustrated in Fig. 2. In CAC simulations, we first address which specific looping mechanism occurs for each dislocation bypass in a sequence of dislocation interactions with the precipitate. The first set of simulations considers the interactions of the array of moving dislocations with the largest precipitate studied in this work ($D = 5.6$ nm). Fig. 10 shows that the outcome of the interaction with the first dislocation is to form an Orowan loop. Since the first dislocation has an edge character, the character of the parts of the loop on the incoming and outgoing sides are primarily edge-oriented and the remaining parts on the lateral sides of the precipitate are screw-oriented. When the second edge dislocation approaches the precipitate, it bows around the precipitate much like the first one; however, in this case, the segments of the second dislocation that wrap around the precipitate cause the screw components of the Orowan loop, left by the first dislocation, to double cross slip above the glide plane (the compressive side of the original dislocation array), as shown in Fig. 11(b). Cross-slipped dislocation segments on the two sides of the precipitate subsequently annihilate (Fig. 11(c)), forming an interstitial type prismatic loop on the incoming side of the precipitate and a vacancy type prismatic loop on the outgoing side. The screw components of the second edge dislocation start to double cross slip as well, but toward the tensile side of the dislocation, leading to the formation of another pair of prismatic loops — again one of interstitial and another of vacancy type (Fig. 11(d−e)). The cross-slip distance is just long enough to overcome the obstacle height, so the diameter of each prismatic loop is roughly $D/2$. Overall, bypass of the second dislocation removes the Orowan loop left by the first dislocation and creates four prismatic loops that can glide away. The second dislocation glides away undamaged and does not contain jogs, clearing the periphery of the precipitate of defects. The observed bypass mechanism agrees with a prior MS simulation [24] but contrasts with the original Hirsch looping mechanism [12] in which the pre-existing Orowan loop is expected to remain intact.

Subsequent bypassing dislocations would need to first interact with the prismatic loops produced by the first two dislocations. As
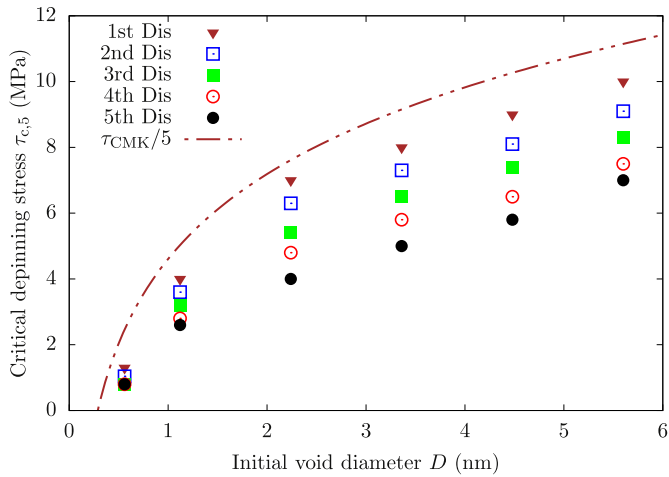
(a)
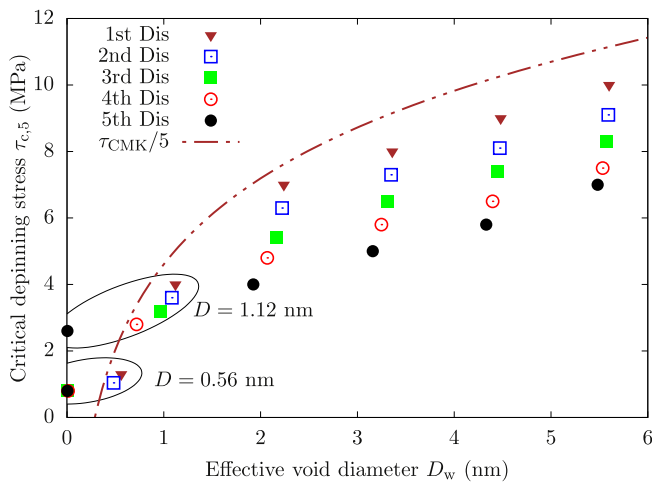
(b)

Fig. 9. CAC-based depinning stress taken at each dislocation exiting the void when $N_{dis} = 5$, with respect to (a) the initial void diameter D and (b) the effective void diameter D_w. The predictions by Eq. (13) are also shown.

quantification, MD simulations for a precipitate with size $D = 3$ nm have reported the critical stress for dislocation/prismatic loop interactions to be one third that for dislocation/precipitate interactions [25]. It follows that the dislocation bypasses the precipitate, leaving an Orowan shear loop around it, repeating the same mechanism that was observed in the first dislocation/precipitate interaction. The fourth dislocation bypasses the precipitate following the Hirsch looping mechanism, transforming the newly formed Orowan loop into two prismatic loops, in the same manner

as the second dislocation/precipitate interaction. As a result, after the fourth dislocation interaction, no shear loop remains around the precipitate. Interaction with the fifth dislocation forms the Orowan loop, as the first and third dislocations had done. Evidently, these simulations have identified an alternating bypass-pattern, consisting of defect formation followed by 'healing'. Table 2 illustrates the alternating Orowan and Hirsch looping mechanisms for sequential dislocation/impenetrable precipitate interactions. We find that this bypass mechanism prevails for all precipitate sizes that are sufficiently large compared to the core size of the dislocation, i.e., $D \geq 1.12$ nm.

As mentioned earlier, the sizes of the Orowan and prismatic loops formed by each bypass scale with the precipitate diameter D. An interesting case, therefore, arises when D is on the order of the dislocation core width, i.e., $D = 0.56$ nm and the precipitate contains only seven atoms. Previous electronic structure calculations showed that a vacancy cluster consisting of only a few vacancies has a lower binding energy than a prismatic loop of vacancy type containing the same number of vacancies [58]. Thus, it is expected that if the Hirsch looping occurred for this small precipitate, point defect clusters of similar size would form in lieu of prismatic loops. In CAC simulations, the first dislocation bypasses the precipitate with $D = 0.56$ nm creating two self-interstitials and two vacancies, as shown in Fig. 12. This suggests that the bypass followed a Hirsch looping-like mechanism. All subsequent dislocation bypasses follow the same Hirsch looping-like mechanism, leaving behind a series of vacancy and interstitial point defect clusters.

A question then arises as why the Orowan looping, which was found for all interactions of the first dislocation in the array when $D \geq 1.12$ nm, did not take place. As discussed in Section 1, Hatano [25] found that the edge dislocation bypassing is more susceptible to Hirsch looping if the local stress field is asymmetric with respect to the glide plane, which may occur if h is too large. Indeed, when $D = 0.56$ nm, it is geometrically impossible to center the precipitate on the glide plane. We found that $h = d_{111}/2$ and hence $h/D = 0.21$, which is large enough to trigger screw dislocation cross-slip and hence the Hirsch looping mechanism [20]. By comparison, the precipitates with $D \geq 1.12$ nm are sufficiently large to be centered very close to the slip plane, resulting in a near-symmetric stress field that favors Orowan looping for the first dislocation. We note that as a practical matter for dislocations interaction with fields of obstacles in a crystal, asymmetry should be expected to be rather prevalent.

After revealing the sequence of looping mechanisms involved in bypassing a precipitate by a dislocation array, we turn our attention to the depinning stress. To the best of our knowledge, the SB model (Eq. (8)) is the only available continuum model for dislocation/precipitate interactions. To account for the long-range effect of the dislocation array, we follow Eq. (12) and divide Eq. (8) by N_{dis}, i.e.,

$$\tau_{SB, N_{dis}} = \frac{\tau_{SB}}{N_{dis}} = \frac{\mu b}{2\pi N_{dis} L} \ln\left(\frac{\overline{D}}{b} + \Delta\right) \tag{14}$$
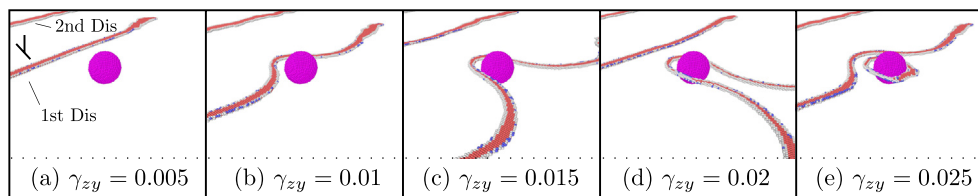

Fig. 10. Snapshots of the first edge dislocation bypassing an impenetrable precipitate with $D = 5.6$ nm following the Orowan looping mechanism. In (b–d), the dislocation bows around the precipitate; in (e), the dislocation glides away with a shear loop left behind. Atoms on the precipitate surface are rendered in magenta.
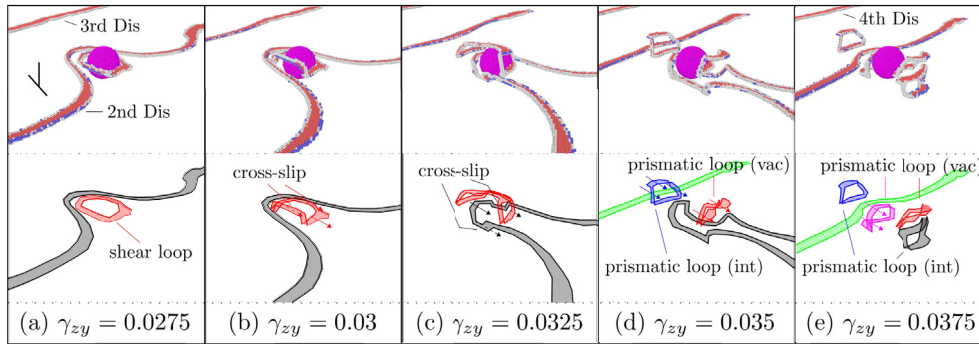
Fig. 11. Snapshots of the second edge dislocation bypassing an impenetrable precipitate with $D = 5.6$ nm following the Hirsch looping mechanism. In the first row, atoms on the precipitate surface are rendered in magenta. In the second row, different dislocations are distinguished by colors. (For interpretation of the references to color in this figure legend, the reader is referred to the Web version of this article.)

Table 2
Alternating Orowan and Hirsch looping mechanisms of sequential dislocation bypass of an impenetrable precipitate when $D \geq 1.12$ nm. Shear loops, prismatic loops of interstitial type, and prismatic loops of vacancy type, are in red, black, and blue, respectively. The slip plane of the edge dislocation array is in grey.

N_{by}	Bypass mechanism	Result
1	Orowan looping	1 shear loop
2	Hirsch looping	4 prismatic loops
3	Orowan looping	4 prismatic loops +1 shear loop
4	Hirsch looping	8 prismatic loops
5	Orowan looping	8 prismatic loops +1 shear loop

where $\Delta = 0.7$ [59]. Fig. 13(a) shows that, for the first dislocation bypass, $\tau_{SB,N_{dis}}$ better predicts the depinning stress when $N_{dis} > 1$ than τ_{SB}. In addition, compared to the CMK model (Eq. (9)) for dislocation/void interactions, predictions based on the SB model deviate more from CAC-predicted depinning stress for dislocation/precipitate interactions, $\tau_{c,N_{dis}}$, especially when the precipitate is small. Previous atomistic studies also showed that the SB-type model yields better predictions when the obstacle is a void than

when it is a precipitate [60].

When $N_{dis} > 1$, subsequent dislocation bypass events follow an alternating Orowan and Hirsch looping mechanism, as described earlier. In contrast to the case of a void, the morphology of the impenetrable precipitate is not changed by glide dislocations. In the meantime, the force applied on the leading dislocation by other dislocations in its wake, $\mathbf{F}_{dis}$, decreases after each dislocation bypass. As a result, the depinning stress $\tau_{c,N_{dis}}$ is expected to increase as more dislocations glide to the outgoing side. Our CAC simulation results, shown in Fig. 13(b), confirm this hypothesis. We note that each dislocation bypass, following either Orowan or Hirsch mechanism, requires similar $\tau_{c,N_{dis}}$, if the effects of the dislocation pile-up were excluded. More specifically, for the same precipitate diameter, the depinning stresses for the fifth dislocation when $N_{dis} = 5$ (the black filled circles in Fig. 13(b)) are close to those for the first dislocation when $N_{dis} = 1$ (the black filled circles in Fig. 13(a)). This result agrees with previous MD [23] and MS simulations [24], in which the depinning stress for Hirsch looping was a few percent lower than that for Orowan looping. In these atomistic simulations, however, the second dislocation was introduced into the system after the first dislocation had bypassed the obstacle, so long-range effects were not involved.

3.3. Further discussions

Our results reveal that the interaction of an obstacle with an array of moving dislocations cannot be understood on the basis of only a single dislocation/obstacle interaction. The mechanisms involved in sequential bypass by an array of dislocations do not lead to defect accumulation around the obstacle or in the gliding dislocations. When the obstacle is a void, it becomes a progressively weaker barrier to subsequent dislocation bypass; with a sufficient number of dislocation passages, it is eventually split into two smaller voids. When the obstacle is a sufficiently large impenetrable precipitate, the residual defect left by the first dislocation is removed by the second dislocation. More importantly we show that
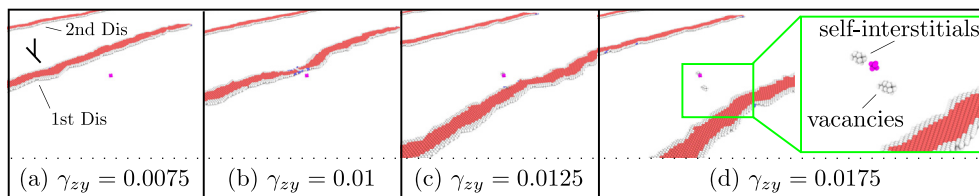

Fig. 12. Snapshots of the first edge dislocation bypassing an impenetrable precipitate with $D = 0.56$ nm following the Hirsch looping mechanism. In (d), two self-interstitials and two vacancies are formed in the vicinity of the precipitate. Atoms on the precipitate surface are rendered in magenta.
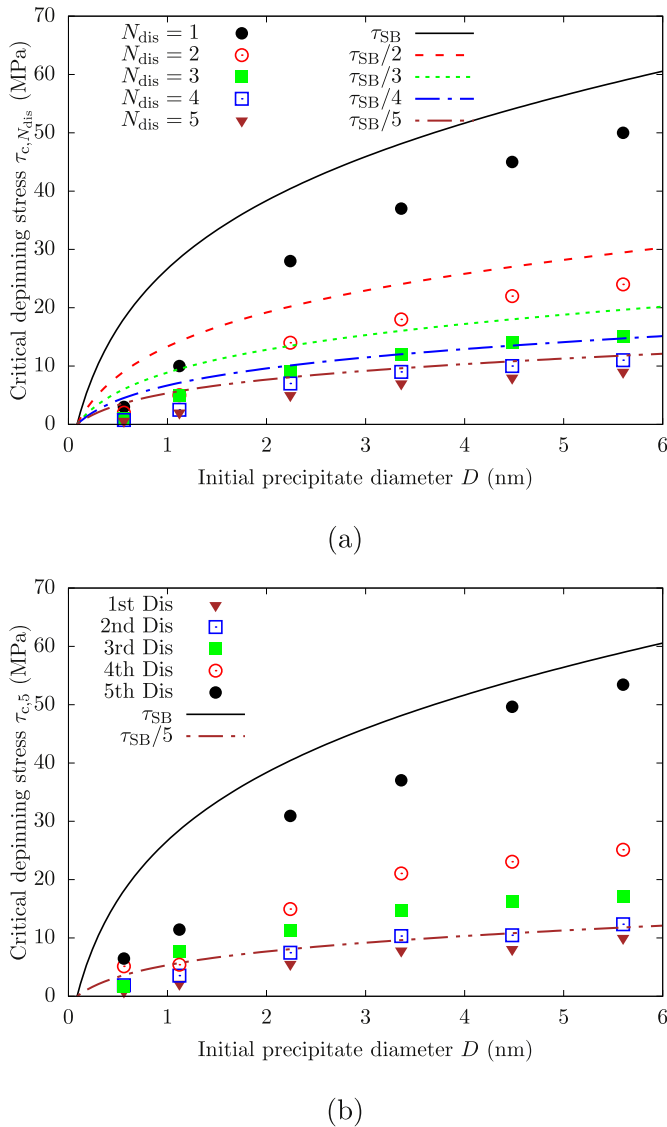
(a)

(b)

Fig. 13. CAC-based depinning stress taken at each dislocation exiting the impenetrable precipitate taken (a) at the first dislocation exiting the precipitate when N_{dis} varies from 1 to 5 and (b) at each dislocation exiting the precipitate when $N_{dis} = 5$. The predictions by Eq. (14) (with $\Delta = 0.7$) are also shown.

this alternating sequence can repeat on a continuing basis since the prismatic loops that are created in the process do not pose significant barriers to the impinging dislocation array. This suggests that in this case the nanoprecipitate resistance to dislocation bypass does not increase with the number of dislocation bypass interactions, in contrast to the conventional understanding that a growing back stress arises from layered Orowan loops and results in strain hardening. With the alternating dislocation bypass mechanism found here, the back stress would remain almost invariant as the number of bypass dislocation events increases. Since the Orowan loop is the main contributor to the Bauschinger effect in precipitation strengthened materials [61], the transformation of the Orowan loop into prismatic loops reduces the subsequent strain hardening and diminishes the Bauschinger effect [62]. Our finding may in part explain why, in incrementally pre-strained materials, the Bauschinger effect parameter converges to a constant for large pre-strain [63].

In dislocation/precipitate interactions, a key unit process is

cross-slip of the side screw segments of the Orowan loop. It can be further envisioned that the alternating pattern in Table 2 will be followed once the cross-slip is initiated, regardless of the maximum number of stable layered Orowan loops allowed to form. Our calculations involve nano-sized precipitates but it is possible that interactions with larger, submicron ones may involve similar sequences of events but with higher energetic requirements for the dislocation to travel around or over (double cross-slip) a larger surface. Stochastic cross-slip-equipped DDD simulations of sequential screw dislocations bypassing an impenetrable precipitate ($D = 524$ nm) in Cu showed that cross-slip occurs when there are more than three layered Orowan loops [19]. In our simulations involving edge dislocations and much smaller precipitates, the maximum number of stable Orowan loops is 1.

The current study did not examine effects of material properties, misfit between the matrix and precipitate (e.g., coherency/image stresses), temperature, strain rate, or dislocation spacing, all of which affect the probability for dislocations to climb and cross-slip, and hence the dislocation/precipitate interactions found here. For cross slip, the dislocation core needs to constrict and this is a thermally activated process. It has been identified that a higher ISFE [9], higher coherency/image stresses [19,21], and higher temperature/strain rate [64] increase the likelihood of dislocation cross-slip when a dislocation impinges on either a void or a precipitate. These findings suggest an anomalous higher bypass stress with higher temperature and suggest that the healing bypass mechanisms reported in this paper might be promoted in usual experiments involving coherency/image stresses, higher temperatures, and lower strain rates.

The dislocations considered in this work are initially straight and of pure edge character, and they are driven to sequentially interact with an obstacle. Other character dislocations, such as screw and mixed, may yield different interaction results. Nevertheless, in our simulations, an edge dislocation reorients to a mixed or screw character in the vicinity of the obstacle. Thus, our choice of initially edge dislocations presents a myriad of interesting possible sequential bypass mechanisms. In contrast, a screw dislocation, or a mixed-type dislocation with dominant screw character, may predictably double cross-slip over an impenetrable precipitate [33], but this remains to be seen. It would also be beneficial to explore the problem of multiple dislocations gliding in materials containing a random distribution of various types of obstacle [65].

4. Conclusions

In summary, we employ a multiscale CAC method to reveal the mechanisms by which a planar array of five glide dislocations with Burgers vector magnitude b interact with a spherical obstacle of nanoscale diameter D in FCC Al. When the obstacle is a void, all dislocations sequentially shear the void into two hemispheres until the void becomes fully split into two separate pieces which pose less significant barriers to subsequent dislocation motion. The number of dislocations required to achieve this is $\lceil D/b \rceil$. This bypass mechanism implies that the barrier strength of a void is dominated by its interaction with the first dislocation in the array and by its size. Based on the new insight gained we present an analytical model to predict the depinning stress for the first dislocation. When the obstacle is an impenetrable precipitate centered on the glide plane, an alternating Orowan and Hirsch looping mechanism occurs. The first, third, and fifth dislocations leave behind a shear loop around the precipitate while the second and fourth dislocations transform the newly formed Orowan loop into two prismatic loops, with itself bypassing the precipitate following the Hirsch looping mechanism. This sequence suggests that after the bypass by a series of successive dislocations, defects do not accumulate

around the precipitate, unlike the classical case of a single dislocation/precipitate interaction. Also contrary to prior studies, defects are not created in the dislocations that glide away. These results are substantial in suggesting reconsideration of conventional thought on the role of voids and precipitates in strain hardening and hysteresis behavior in cyclic loading. The new understanding attained in this work can benefit model-guided design of materials that develop voids due to irradiation, or precipitates due to alloying.

Acknowledgments

Appendix A. Model validation

Because voids and traction-free simulation cell boundaries may act as sources for dislocations [66–69], it is important to ensure in our simulations that no dislocation other than those in the pre-existing array is nucleated. To this end, simulation cells containing an obstacle but no dislocation array are investigated. In the case of a void, dislocations are homogeneously nucleated inside the system when $D = 0.56$ and 1.12 nm, while dislocations are nucleated from the void surface for larger D, as shown in Fig. A1. The same change in the dislocation nucleation mode as D increases was also reported in previous MD simulations of nanovoid growth in Cu [70], V [71], and Ta [72]. In our work, among all D, the lowest applied shear strain γ_{zy} for dislocation nucleation is 0.102. In the case of an impenetrable precipitate, no dislocation is nucleated with the shear strain up to $\gamma_{zy} = 0.13$. In our simulations, all five glide dislocations in the array have bypassed the obstacle by $\gamma_{zy} = 0.1$.
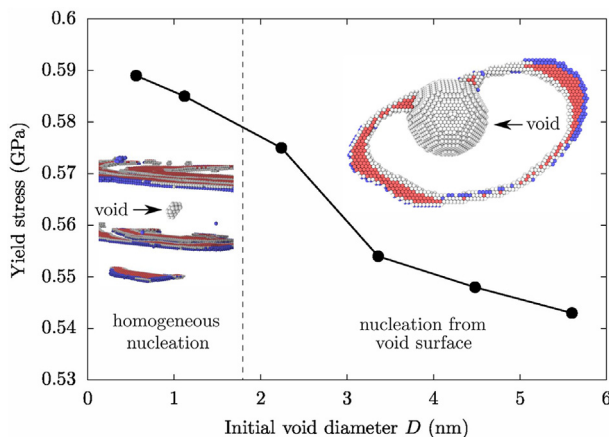

Fig. A1. Yield stress with respect to the initial void diameter D for simulation cells containing a void but no pre-existing dislocation. When $D = 0.56$ and 1.12 nm, dislocations are nucleated homogeneously in the material; for larger D, dislocations are nucleated from the void surface. The two insets are for $D = 0.56$ and 5.6 nm, taken on the threshold of plasticity at $\gamma_{zy} = 0.12$ and 0.102, respectively.

In addition, as the D'/D ratio is fixed for the same type of obstacle, the size of the atomistic domain D' around the obstacle increases with the obstacle size D. The question then arises as to whether the choice of D' affects the simulation results. To this end, simulation cells containing an array of five pre-existing dislocations but no obstacle are studied, with D' varying from 2.24 to 17.92 nm. Fig. A2 shows that the stress-strain curves for different D' are close to each other, while the stacking fault width in the atomistic domain is smaller than that in the coarse-grained domain, in agreement with previous CAC simulations [37]. This suggests that resolving an atomistic domain in a certain region does not significantly alter the stress-strain response or the dislocation motion.
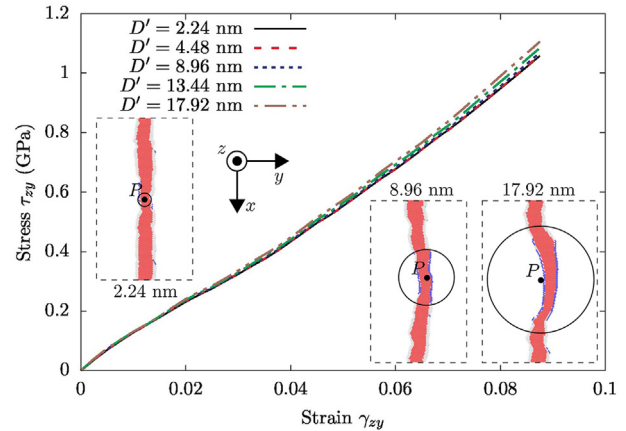

Fig. A2. Stress-strain curves of the simulation cells containing an array of five pre-existing dislocations but no obstacle. In each case, an atomistic domain is resolved within the sphere centered at P with diameter D'. The curves for different D' are close to each other. The three insets, which show the first edge dislocation configurations at $\gamma_{zy} = 0.01$, are for $D' = 2.24$, 8.96, and 17.92 nm, respectively. The view is illustrated by the coordinate system. The extended dislocation is found to have a smaller stacking fault width in the atomistic domain than in the coarse-grained domain, as expected [42].

Appendix B. Timestep size validation

To explore the effect of the timestep size Δt, we perform additional CAC simulations with $\Delta t = 1$ and 2 fs, respectively, when $N_{dis} = 5$ and $D = 5.6$ nm. In the case of a void, the depinning stresses τ_c taken at each dislocation bypass are found to be similar to those predicted with $\Delta t = 5$ fs, as shown in Fig. B1.
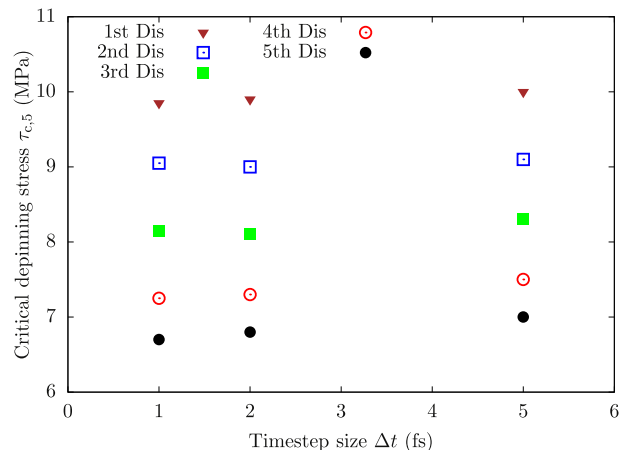

Fig. B1. CAC-based depinning stress as a function of the timestep size Δt at each dislocation exiting the void when $N_{dis} = 5$ and $D = 5.6$ nm.

In the case of an impenetrable precipitate, the alternating Orowan and Hirsch looping mechanisms were also observed with two smaller Δt. These suggest that the timestep size $\Delta t = 5$ fs used in

our CAC simulations is sufficient for time integration.

References

[1] L. Xiong, S. Xu, D.L. McDowell, Y. Chen, Concurrent atomistic-continuum simulations of dislocation-void interactions in fcc crystals, Int. J. Plast. 65 (2015) 33—42, https://doi.org/10.1016/j.ijplas.2014.08.002. URL, http://www.sciencedirect.com/science/article/pii/S0749641914001508.

[2] A. Patra, D.L. McDowell, Crystal plasticity-based constitutive modelling of irradiated bcc structures, Philos. Mag. A 92 (7) (2012) 861—887, https://doi.org/10.1080/14786435.2011.634855. URL, https://doi.org/10.1080/14786435.2011.634855.

[3] D.J. Bacon, Y.N. Osetsky, D. Rodney, Dislocation-obstacle interactions at the atomic level, in: L. Kubin, J.P. Hirth (Eds.), Dislocations in Solids, vol. 15, Elsevier, 2009, pp. 1—90. URL, http://www.sciencedirect.com/science/article/pii/S1572485909015010.

[4] A. Dutta, M. Bhattacharya, N. Gayathri, G.C. Das, P. Barat, The mechanism of climb in dislocation-nanovoid interaction, Acta Mater. 60 (9) (2012) 3789—3798, https://doi.org/10.1016/j.actamat.2012.03.050. URL, http://www.sciencedirect.com/science/article/pii/S1359645412002406.

[5] Y.N. Osetsky, D.J. Bacon, Comparison of void strengthening in fcc and bcc metals: large-scale atomic-level modelling, Mater. Sci. Eng. A 400—401 (2005) 374—377, https://doi.org/10.1016/j.msea.2005.02.083. URLhttp://www.sciencedirect.com/science/article/pii/S0921509305003497.

[6] D.J. Bacon, Y.N. Osetsky, Modelling dislocation-obstacle interactions in metals exposed to an irradiation environment, Mater. Sci. Eng. A 400—401 (2005) 353—361, https://doi.org/10.1016/j.msea.2005.01.061. URLhttp://www.sciencedirect.com/science/article/pii/S0921509305003084.

[7] S. Sarkar, J. Li, W.T. Cox, E. Bitzek, T.J. Lenosky, Y. Wang, Finding activation pathway of coupled displacive-diffusional defect processes in atomistics: dislocation climb in fcc copper, Phys. Rev. B 86 (1) (2012) 014115, https://doi.org/10.1103/PhysRevB.86.014115. URL, https://link.aps.org/doi/10.1103/PhysRevB.86.014115.

[8] T. Okita, K. Asari, S. Fujita, M. Itakura, Effect of the stacking fault energy on interactions between an edge dislocation and a spherical void in FCC metals at various spatial geometries, Fusion Sci. Technol. 66 (1) (2014) 289—294, https://doi.org/10.13182/FST13-756. URL, https://doi.org/10.13182/FST13-756.

[9] K. Doihara, T. Okita, M. Itakura, M. Aichi, K. Suzuki, Atomic simulations to evaluate effects of stacking fault energy on interactions between edge dislocation and spherical void in face-centred cubic metals, Philos. Mag. A 98 (22) (2018) 2061—2076, https://doi.org/10.1080/14786435.2018.1472401. URL, https://doi.org/10.1080/14786435.2018.1472401.

[10] N. Mott, F. Nabarro, Report of a Conference on Strength of Solids, vol. 1, Physical Society, 1948.

[11] J.W. Martin, Precipitation Hardening, second ed., Butterworth-Heinemann, 1998.

[12] F.J. Humphreys, P.B. Hirsch, The deformation of single crystals of copper and copper-zinc alloys containing alumina particles. II. Microstructure and dislocation-particle interactions, Proc. Phys. Soc., London 318 (1532) (1970) 73—92, https://doi.org/10.1098/rspa.1970.0134. URL, http://rspa.royalsocietypublishing.org/content/318/1532/73.

[13] P.M. Hazzledine, P.B. Hirsch, A critical examination of the long-range stress theory of work-hardening, Philos. Mag. A 15 (133) (1967) 121—159, https://doi.org/10.1080/14786436708230354. URL, https://doi.org/10.1080/14786436708230354.

[14] L.M. Brown, W.M. Stobbs, The work-hardening of copper-silica, Philos. Mag. A 23 (185) (1971) 1201—1233, https://doi.org/10.1080/14786437108217406. URL, https://doi.org/10.1080/14786437108217406.

[15] A.M. Wusatowska-Sarnek, H. Miura, T. Sakai, Coherency strains influence on martensitic transformation of γ-Fe particles in compressed Cu-Fe alloy single crystals, J. Mater. Sci. 34 (22) (1999) 5477—5487, https://doi.org/10.1023/A:1004748125256. URL https://link.springer.com/article/10.1023/A:1004748125256.

[16] A. Lehtinen, F. Granberg, L. Laurson, K. Nordlund, M.J. Alava, Multiscale modeling of dislocation-precipitate interactions in Fe: from molecular dynamics to discrete dislocations, Phys. Rev. E 93 (1) (2016) 013309, https://doi.org/10.1103/PhysRevE.93.013309. URL, http://link.aps.org/doi/10.1103/PhysRevE.93.013309.

[17] P. Paus, M. Benes, M. Kolár, J. Kratochvíl, Dynamics of dislocations described as evolving curves interacting with obstacles, Model. Simul. Mater. Sci. Eng. 24 (3) (2016) 035003, https://doi.org/10.1088/0965-0393/24/3/035003. URL, http://stacks.iop.org/0965-0393/24/i=3/a=035003.

[18] R. Santos-Güemes, G. Esteban-Manzanares, I. Papadimitriou, J. Segurado, L. Capolungo, J. LLorca, Discrete dislocation dynamics simulations of dislocation-θ' precipitate interaction in Al-Cu alloys, J. Mech. Phys. Solids 118 (2018) 228—244, https://doi.org/10.1016/j.jmps.2018.05.015. URL https://www.sciencedirect.com/science/article/pii/S0022509617310037.

[19] C.S. Shin, M.C. Fivel, M. Verdier, K.H. Oh, Dislocation-impenetrable precipitate interaction: a three-dimensional discrete dislocation dynamics analysis, Philos. Mag. A 83 (31—34) (2003) 3691—3704, https://doi.org/10.1080/14786430310001599379. URL, https://doi.org/10.1080/14786430310001599379.

[20] Y. Xiang, D.J. Srolovitz, L.T. Cheng, W. E, Level set simulations of dislocation-

[21] Y. Xiang, D.J. Srolovitz, Dislocation climb effects on particle bypass mechanisms, Philos. Mag. A 86 (25—26) (2006) 3937—3957, https://doi.org/10.1080/14786430600575427. URL, https://doi.org/10.1080/14786430600575427.

[22] M.E. Krug, D.C. Dunand, Modeling the creep threshold stress due to climb of a dislocation in the stress field of a misfitting precipitate, Acta Mater. 59 (13) (2011) 5125—5134, https://doi.org/10.1016/j.actamat.2011.04.044. URL, http://www.sciencedirect.com/science/article/pii/S1359645411003004.

[23] L. Proville, B. Bakó, Dislocation depinning from ordered nanophases in a model fcc crystal: from cutting mechanism to Orowan looping, Acta Mater. 58 (17) (2010) 5565—5571, https://doi.org/10.1016/j.actamat.2010.06.018. URL, http://www.sciencedirect.com/science/article/pii/S1359645410003721.

[24] S. Groh, Transformation of shear loop into prismatic loops during bypass of an array of impenetrable particles by edge dislocations, Mater. Sci. Eng. A 618 (2014) 29—36, https://doi.org/10.1016/j.msea.2014.08.079. URLhttp://www.sciencedirect.com/science/article/pii/S0921509314010880.

[25] T. Hatano, Dynamics of a dislocation bypassing an impenetrable precipitate: the Hirsch mechanism revisited, Phys. Rev. B 74 (2) (2006) 020102, https://doi.org/10.1103/PhysRevB.74.020102. URL, http://link.aps.org/doi/10.1103/PhysRevB.74.020102.

[26] S. Xu, X. Chen, Modeling dislocations and heat conduction in crystalline materials: atomistic/continuum coupling approaches, Int. Mater. Rev. (2019). https://doi.org/10.1080/09506608.2018.1486358.

[27] S.Z. Chavoshi, S. Xu, Nanoindentation/scratching at finite temperatures: insights from atomistic-based modeling, Prog. Mater. Sci. 100 (2019) 1—20, https://doi.org/10.1016/j.pmatsci.2018.09.002. URL, http://www.sciencedirect.com/science/article/pii/S0079642518300914.

[28] S. Xu, L. Xiong, Y. Chen, D.L. McDowell, Shear stress- and line length-dependent screw dislocation cross-slip in FCC Ni, Acta Mater. 122 (2017) 412—419, https://doi.org/10.1016/j.actamat.2016.10.005. URL, http://www.sciencedirect.com/science/article/pii/S1359645416307601.

[29] S. Xu, J. Rigelesaiyin, L. Xiong, Y. Chen, D.L. McDowell, Generalized continua concepts in coarse-graining atomistic simulations, in: H. Altenbach, J. Pouget, M. Rousseau, B. Collet, T. Michelitsch (Eds.), Generalized Models and Non-classical Approaches in Complex Materials 2, Advanced Structured Materials, Springer International Publishing, 2018, pp. 237—260.

[30] S. Xu, M.I. Latypov, Y. Su, Concurrent atomistic-continuum simulations of uniaxial compression of gold nano/submicropillars, Phil. Mag. Lett. 98 (5) (2018) 173—182, https://doi.org/10.1080/09500839.2018.1515506. URL, https://doi.org/10.1080/09500839.2018.1515506.

[31] S. Xu, L. Xiong, Y. Chen, D.L. McDowell, Sequential slip transfer of mixed-character dislocations across ∑3 coherent twin boundary in FCC metals: a concurrent atomistic-continuum study, npj Comput. Mater 2 (2016) 15016, https://doi.org/10.1038/npjcompumats.2015.16. URL http://www.nature.com/articles/npjcompumats201516.

[32] S. Xu, L. Xiong, Y. Chen, D.L. McDowell, Comparing EAM potentials to model slip transfer of sequential mixed character dislocations across two symmetric tilt grain boundaries in Ni, JOM 69 (5) (2017) 814—821, https://doi.org/10.1007/s11837-017-2302-1. URL, https://link.springer.com/article/10.1007/s11837-017-2302-1.

[33] C.V. Singh, A.J. Mateos, D.H. Warner, Atomistic simulations of dislocation-precipitate interactions emphasize importance of cross-slip, Scripta Mater. 64 (5) (2011) 398—401, https://doi.org/10.1016/j.scriptamat.2010.10.041. URL, http://www.sciencedirect.com/science/article/pii/S135964621000074X.

[34] G. Esteban-Manzanares, E. Martínez, J. Segurado, L. Capolungo, J. LLorca, An atomistic investigation of the interaction of dislocations with Guinier-Preston zones in Al-Cu alloys, Acta Mater. 162 (2019) 189—201, https://doi.org/10.1016/j.actamat.2018.09.052. URL, http://www.sciencedirect.com/science/article/pii/S135964541830764X.

[35] S. Xu, Modelling plastic deformation of nano/submicron-sized tungsten pillars under compression: a coarse-grained atomistic approach, Int. J. Multiscale Comput. Eng. 16 (4) (2018) 367—376, https://doi.org/10.1615/IntJMultCompEng.2018026027. URL, http://www.dl.begellhouse.com/journals/61fd1b191cf7e96f,77bb56c9113fd8ad,519a0e1634b8eddd.html.

[36] Y. Chen, Reformulation of microscopic balance equations for multiscale materials modeling, J. Chem. Phys. 130 (13) (2009) 134706, https://doi.org/10.1063/1.3103887. URL, http://jcp.aip.org/resource/1/jcpsa6/v130/i13/p134706_s1.

[37] S. Xu, R. Che, L. Xiong, Y. Chen, D.L. McDowell, A quasistatic implementation of the concurrent atomistic-continuum method for FCC crystals, Int. J. Plast. 72 (2015) 91—126, https://doi.org/10.1016/j.ijplas.2015.05.007. URL, http://www.sciencedirect.com/science/article/pii/S0749641915000777.

[38] S. Xu, L. Xiong, Q. Deng, D.L. McDowell, Mesh refinement schemes for the concurrent atomistic-continuum method, Int. J. Solids Struct. 90 (2016) 144—152, https://doi.org/10.1016/j.ijsolstr.2016.03.030. URL, http://www.sciencedirect.com/science/article/pii/S0020768316300154.

[39] V. Bulatov, W. Cai, Computer Simulations of Dislocations, Oxford University Press, Oxford ; New York, 2006.

[40] S. Xu, J.R. Mianroodi, A. Hunter, I.J. Beyerlein, B. Svendsen, Phase-field-based calculations of the disregistry fields of static extended dislocations in FCC metals, Philos. Mag. A 99 (11) (2019) 1400—1428, https://doi.org/10.1080/14786435.2019.1582850. URL, https://doi.org/10.1080/14786435.2019.1582850.

[41] Y. Mishin, D. Farkas, M.J. Mehl, D.A. Papaconstantopoulos, Interatomic potentials for monoatomic metals from experimental data and *ab initio* calculations, Phys. Rev. B 59 (5) (1999) 3393–3407, https://doi.org/10.1103/PhysRevB.59.3393. URL, http://link.aps.org/doi/10.1103/PhysRevB.59.3393.

[42] S. Xu, T.G. Payne, H. Chen, Y. Liu, L. Xiong, Y. Chen, D.L. McDowell, PyCAC: the concurrent atomistic-continuum simulation environment, J. Mater. Res. 33 (7) (2018) 857–871, https://doi.org/10.1557/jmr.2018.8. URL, https://www.cambridge.org/core/journals/journal-of-materials-research/article/pycac-the-concurrent-atomisticcontinuum-simulation-environment/E664F7A8C0AD8DD1673BE2BDE592D0AA.

[43] S. Xu, PyCAC User's Manual, Aug. 2017. http://www.pycac.org/. (Accessed 17 May 2019).

[44] A. Stukowski, Visualization and analysis of atomistic simulation data with OVITO—the Open Visualization Tool, Model. Simul. Mater. Sci. Eng. 18 (1) (2010) 015012, https://doi.org/10.1088/0965-0393/18/1/015012. URL, http://iopscience.iop.org/0965-0393/18/1/015012.

[45] A. Stukowski, Structure identification methods for atomistic simulations of crystalline materials, Model. Simul. Mater. Sci. Eng. 20 (4) (2012) 045021, https://doi.org/10.1088/0965-0393/20/4/045021. URL, http://iopscience.iop.org/0965-0393/20/4/045021.

[46] M. Bahramyan, R.T. Mousavian, D. Brabazon, Molecular dynamic simulation of edge dislocation-void interaction in pure Al and Al-Mg alloy, Mater. Sci. Eng. A 674 (2016) 82–90, https://doi.org/10.1016/j.msea.2016.07.121. URL, http://www.sciencedirect.com/science/article/pii/S0921509316308966.

[47] A.J.E. Foreman, M.J. Makin, Dislocation movement through random arrays of obstacles, Philos. Mag. A 14 (131) (1966) 911–924, https://doi.org/10.1080/14786436608244762. URL, https://doi.org/10.1080/14786436608244762.

[48] E. Bitzek, P. Gumbsch, Dynamic aspects of dislocation motion: atomistic simulations, Mater. Sci. Eng. A 400–401 (2005) 40–44, https://doi.org/10.1016/j.msea.2005.03.047. URLhttp://www.sciencedirect.com/science/article/pii/S0921509305002571.

[49] M. Peach, J.S. Koehler, The forces exerted on dislocations and the stress fields produced by them, Phys. Rev. 80 (3) (1950) 436–439, https://doi.org/10.1103/PhysRev.80.436. URL, https://link.aps.org/doi/10.1103/PhysRev.80.436.

[50] A.J.E. Foreman, Dislocation energies in anisotropic crystals, Acta Metall. 3 (4) (1955) 322–330, https://doi.org/10.1016/0001-6160(55)90036-5. URL, http://www.sciencedirect.com/science/article/pii/0001616055900365.

[51] D.J. Bacon, U.F. Kocks, R.O. Scattergood, The effect of dislocation self-interaction on the Orowan stress, Philos. Mag. A 28 (6) (1973) 1241–1263, https://doi.org/10.1080/14786437308227997. URL, https://doi.org/10.1080/14786437308227997.

[52] R.O. Scattergood, D.J. Bacon, The Orowan mechanism in anisotropic crystals, Philos. Mag. A 31 (1) (1975) 179–198, https://doi.org/10.1080/14786437508229295. URL, https://doi.org/10.1080/14786437508229295.

[53] R.O. Scattergood, D.J. Bacon, The strengthening effect of voids, Acta Metall. 30 (8) (1982) 1665–1677, https://doi.org/10.1016/0001-6160(82)90188-2. URL, http://www.sciencedirect.com/science/article/pii/0001616082901882.

[54] J.C. Crone, L.B. Munday, J. Knap, Capturing the effects of free surfaces on void strengthening with dislocation dynamics, Acta Mater. 101 (2015) 40–47, https://doi.org/10.1016/j.actamat.2015.08.067. URL, http://www.sciencedirect.com/science/article/pii/S1359645415006540.

[55] S. Xu, L. Xiong, Y. Chen, D.L. McDowell, Edge dislocations bowing out from a row of collinear obstacles in Al, Scripta Mater. 123 (2016) 135–139, https://doi.org/10.1016/j.scriptamat.2016.06.018. URL, http://www.sciencedirect.com/science/article/pii/S135964621630272X.

[56] S. Xu, L. Xiong, Y. Chen, D.L. McDowell, An analysis of key characteristics of the Frank-Read source process in FCC metals, J. Mech. Phys. Solids 96 (2016) 460–476, https://doi.org/10.1016/j.jmps.2016.08.002. URL, http://www.sciencedirect.com/science/article/pii/S0022509616301016.

[57] J.D. Eshelby, F.C. Frank, F.R.N. Nabarro, XLI. The equilibrium of linear arrays of dislocations, London Edinburgh Dublin Philos. Mag. J. Sci. 42 (327) (1951) 351–364, https://doi.org/10.1080/14786445108561060. URL, https://doi.org/10.1080/14786445108561060.

[58] V. Gavini, K. Bhattacharya, M. Ortiz, Vacancy clustering and prismatic dislocation loop formation in aluminum, Phys. Rev. B 76 (18) (2007) 180101, https://doi.org/10.1103/PhysRevB.76.180101. URL, http://link.aps.org/doi/10.1103/PhysRevB.76.180101.

[59] R.O. Scattergood, D.J. Bacon, Dislocation shear loops in anisotropic crystals, Phys. Status Solidi 25 (2) (1974) 395–404, https://doi.org/10.1002/pssa.2210250204. URL, http://onlinelibrary.wiley.com/doi/10.1002/pssa.2210250204/abstract.

[60] Y.N. Osetsky, D.J. Bacon, Void and precipitate strengthening in α-iron: what can we learn from atomic-level modelling? J. Nucl. Mater. 323 (2) (2003) 268–280, https://doi.org/10.1016/j.jnucmat.2003.08.028. URL http://www.sciencedirect.com/science/article/pii/S0022311503003702.

[61] S. Queyreau, B. Devincre, Bauschinger effect in precipitation-strengthened materials: a dislocation dynamics investigation, Phil. Mag. Lett. 89 (7) (2009) 419–430, https://doi.org/10.1080/09500830903005433. URL, https://doi.org/10.1080/09500830903005433.

[62] F. Granberg, D. Terentyev, K. Nordlund, Interaction of dislocations with carbides in BCC Fe studied by molecular dynamics, J. Nucl. Mater. 460 (2015) 23–29, https://doi.org/10.1016/j.jnucmat.2015.01.064. URL, http://www.sciencedirect.com/science/article/pii/S0022311515000811.

[63] H. Kato, K. Sasaki, T. Mori, Four-point bending test of the Bauschinger effect in prestrained IF steel thin sheet, Mater. Sci. Eng. A 642 (2015) 150–156, https://doi.org/10.1016/j.msea.2015.06.075. URL, http://www.sciencedirect.com/science/article/pii/S0921509315301325.

[64] T. Hatano, T. Kaneko, Y. Abe, H. Matsui, Void-induced cross slip of screw dislocations in fcc copper, Phys. Rev. B 77 (6) (2008) 064108, https://doi.org/10.1103/PhysRevB.77.064108. URL, http://link.aps.org/doi/10.1103/PhysRevB.77.064108.

[65] M. Landeiro Dos Reis, L. Proville, M. Sauzay, Modeling the climb-assisted glide of edge dislocations through a random distribution of nanosized vacancy clusters, Phys. Rev. Mater. 2 (9) (2018) 093604, https://doi.org/10.1103/PhysRevMaterials.2.093604. URL, https://link.aps.org/doi/10.1103/PhysRevMaterials.2.093604.

[66] Y. Su, S. Xu, On the role of initial void geometry in plastic deformation of metallic thin films: a molecular dynamics study, Mater. Sci. Eng. A 678 (2016) 153–164, https://doi.org/10.1016/j.msea.2016.09.091. URL, http://www.sciencedirect.com/science/article/pii/S0921509316311741.

[67] S. Xu, Y. Su, Nanovoid growth in BCC α-Fe: influences of initial void geometry, *Modelling Simul.* Mater. Sci. Eng. 24 (8) (2016) 085015, https://doi.org/10.1088/0965-0393/24/8/085015. URL http://stacks.iop.org/0965-0393/24/i=8/a=085015.

[68] S. Xu, Y. Su, D. Chen, L. Li, Plastic deformation of Cu single crystals containing an elliptic cylindrical void, Mater. Lett. 193 (2017) 283–287, https://doi.org/10.1016/j.matlet.2017.02.005. URL, http://www.sciencedirect.com/science/article/pii/S0167577X17301891.

[69] S. Xu, Y. Su, S.Z. Chavoshi, Deformation of periodic nanovoid structures in Mg single crystals, Mater. Res. Express 5 (1) (2018) 016523, https://doi.org/10.1088/2053-1591/aaa678. URL, http://stacks.iop.org/2053-1591/5/i=1/a=016523.

[70] E.M. Bringa, S. Traiviratana, M.A. Meyers, Void initiation in fcc metals: effect of loading orientation and nanocrystalline effects, Acta Mater. 58 (13) (2010) 4458–4477, https://doi.org/10.1016/j.actamat.2010.04.043. URL, http://www.sciencedirect.com/science/article/pii/S1359645410002594.

[71] S.Z. Xu, Z.M. Hao, Y.Q. Su, Y. Yu, Q. Wan, W.J. Hu, An analysis on nanovoid growth in body-centered cubic single crystalline vanadium, Comput. Mater. Sci. 50 (8) (2011) 2411–2421, https://doi.org/10.1016/j.commatsci.2011.03.019. URL, http://www.sciencedirect.com/science/article/pii/S0927025611001625.

[72] Y. Tang, E.M. Bringa, M.A. Meyers, Ductile tensile failure in metals through initiation and growth of nanosized voids, Acta Mater. 60 (12) (2012) 4856–4865, https://doi.org/10.1016/j.actamat.2012.05.030. URL, http://www.sciencedirect.com/science/article/pii/S1359645412003503.